PERGAMON

International Journal of Heat and Mass Transfer 42 (1999) 4081–4091

International Journal of HEAT and MASS TRANSFER

www.elsevier.com/locate/ijhmt

Heat transfer in a swirl chamber at different temperature ratios and Reynolds numbers

C.R. Hedlund[a,1], P.M. Ligrani[a,*], B. Glezer[b], H.-K. Moon[b]

[a]*Convective Heat Transfer Laboratory, Department of Mechanical Engineering, University of Utah, Salt Lake City, UT 84112, USA*
[b]*Solar Turbines Inc., Turbine Cooling Design and Analysis, San Diego, CA 92186, USA*

Received 26 May 1998; received in revised form 5 March 1999

Abstract

Nusselt numbers are presented for a swirl chamber with multiple inlets and helical flow for Reynolds numbers from 6100 to 19,200, and ratios of inlet temperature to wall temperature from 0.60 to 0.95. Local Nusselt numbers, measured over the entire interior surface of the swirl chamber using infrared thermography, are highest near the inlets where important influences from Görtler vortex paris are especially evident. Axially-averaged, circumferentially-averaged, and globally-averaged Nusselt numbers, determined from local values, generally increase as Reynolds number increases and as the temperature ratio decreases.

1. Introduction

Swirl chambers, configured to produce large scale flow rotation, generally about the chamber axis, are used for a wide range of engineering applications. These include segregation of fluids or particles of different density suspended in fluids, increasing mixing in combustion chambers and reaction vessels, increasing the quality at which critical heat flux occurs in two phase flows, and spray-drying applications where an atomizer is used. Swirl chambers are also employed to increase the surface heat and mass transfer levels in a variety of engineering components, ranging from gas turbine engines, automotive engines, furnaces, and heat exchangers, to biomedical devices, and devices for heating and cooling of metal ingots.

Kreith and Margolis [1] initially proposed that swirl induced in tube flows can augment surface heat transfer rates relative to un-swirled flows. Later work [2–7] employed tangential jets from wall slots to induce large-scale swirling in internal tube flows. Swirling flows are also induced in tubes using twisted tape inserts to augment measured surface heat transfer rates [8,9]. Rotating vanes,, blades, propellers, or honeycombs are used near tube entrances in other studies to induce swirl in adiabatic flows [10–12]. Other recent experimental investigations examine fluid mechanics in swirl chambers with single-phase flow, wall injection, and no heat transfer [13–17]. A number of other papers describe surveys of swirl flow investigations [4,18–21].

The present study is different from other swirl chamber investigations because *measured* spatially-resolved surface heat transfer distributions are presented which show the effects of both (i) the ratio of inlet duct temperature to wall temperature, T_i/T_w, and

* Corresponding author. Tel.: +1-801-581-4240; fax: +1-801-585-9826.

E-mail address: ligrani@mech.utah.edu (P.M. Ligrani)

[1] Present address: GE Corporate Research and Development, Schenectady, NY 12301, USA.

0017-9310/99/$ - see front matter
PII: S0017-9310(99)00086-1

Nomenclature

D	swirl chamber inner diameter
D_H	hydraulic diameter of inlet duct
h	heat transfer coefficient
k	thermal conductivity
Nu	Nusselt number, hD/k
r	radial coordinate, measured from swirl chamber centerline
r_o	swirl chamber radius
Re	Reynolds number based on inlet duct characteristics, $\bar{U}D_H/v$
Re_D	Reynolds number based on swirl chamber diameter and axial velocity, $\bar{V}D/v$
T_i	inlet air temperature
T_w	temperature of air adjacent to swirl chamber wall
$\bar{U}$	mean inlet duct velocity
$\bar{V}$	axial average bulk velocity in swirl chamber

Greek symbols

ψ	swirl chamber circumferential location in degrees
v	kinematic viscosity of air

Superscript

–	spatial average

(ii) the Reynolds number, *Re*. Because multiple inlets are employed at fixed locations to induce the swirling, the geometry of our swirl chamber is different from the geometrics used in all existing investigations, except the studies described in Refs. [2–4]. The present study is also unique because spatial variations of local surface Nusselt numbers along swirl chamber surfaces are given, measured using infrared thermography in conjunction with thermocouples, energy balances, digital image processing, and in situ calibration procedures. The local *Nu* values obtained with this approach are averaged in different ways. Circumferentially-averaged surface Nusselt numbers provide information on the axial development of surface heat transfer. Axially-averaged Nusselt numbers are presented which show *Nu* development with circumferential position. Globally-averaged Nusselt numbers then provide a description of overall heat transfer behavior over the range of flow conditions studied. With these data, fundamental information and practical information are provided for a geometry which simulates the internal cooling passage located near the leading edge of a turbine blade.

2. Experimental apparatus and procedures

2.1. Swirl chamber for heat transfer measurements

A schematic of the swirl chamber used for heat transfer measurements is shown in Fig. 1a. The coordinate system is shown in Fig. 1b. The air used within the swirl chamber is circulated in a closed-loop by a Dayton 5CO87-80CFM induced draft blower, which forces air through the facility, starting with a series of three large 1 m square plenums. A Bonneville cross-flow heat exchanger is located between two of these plenums, and is cooled with liquid nitrogen (LN2) at flow rate appropriate to give the desired air temperature at the exit of the heat exchanger. As the air exits

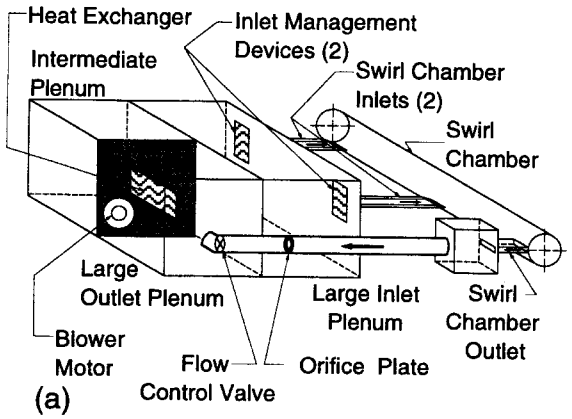

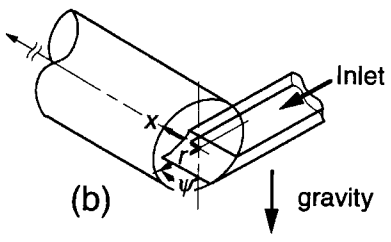

Fig. 1. (a) Schematic of the swirl chamber, and (b) swirl chamber coordinate system.

the heat exchanger, it enters the third plenum, from which the air passes into one of two rectangular bell mouth inlets, each followed by a honeycomb, two screens, and a two-dimensional 10:1 contraction ratio nozzle. Each of the two nozzles leads to a rectangular cross-section inlet duct 21.7 hydraulic diameters in length, connected to the principle swirl chamber cylinder so that one surface is tangent to the cylinder inner circumference. Inlet duct 1 extends axially from $x/r_o=0$ to $x/r_o=1$, and inlet duct 2 extends axially from $x/r_o=7$ to $x/r_o=8$. Both inlet ducts are tangent to the swirl chamber at $\psi=0^\circ$. The cylinder length is 1.43 m, and its inner and outer diameters are 0.191 and 0.203 m, respectively. Because the ratio of the radial extent of the inlet duct to the radius of curvature of the swirl chamber is 0.160, the curvature near cylinder walls is considered to be 'strong'. With this arrangement, the flow has important axial and circumferential components of velocity, and the overall flow pattern through the cylinder is similar to a helix. The exit duct from the cylinder is oriented in a radial/axial plane near the end of the swirl chamber cylinder at a location along the cylinder farthest from the inlet ducts. This exit duct is then connected to a 0.305 m square plenum, which is followed by a pipe containing a valve and an orifice plate, used to regulate and measure the air flow rate, respectively. This pipe is then connected to the same large plenum adjoining the blower inlet.

All exterior and many interior surfaces of the facility are insulated with two to three layers of 2.54 cm thick, Elastomer Products black neoprene foam insulation ($k = 0.038$ W/m K) to minimize heat losses. Calibrated coper-constantan thermocouples are located between the three layers of insulation located outside of the main cylinder of the swirl chamber to determine conduction losses. Between the first layer and the 0.635 cm thick acrylic cylinder of the chamber are 11 custom-made Electrofilm etched-foil heaters (each encapsulated between 2 thin layers of capton) to provide a constant heat flux boundary condition on the concave test surface. The acrylic cylinder contains 30 copper–constantan thermocouples, and its inner surface is adjacent to the air stream. Each of these thermocouples is located 0.0508 cm just below this surface to provide measurements of local surface temperatures, after correction for thermal contact resistance and temperature drop through the 0.050 cm thickness of acrylic. Acrylic is chosen because of its low thermal conductivity ($k = 0.16$ W/m K at 20°C) to minimize axial and circumferential conduction along the test surface, and thus minimize 'smearing' of spatially varying temperature gradients along the test surface. Acrylic also works well for infrared imaging because its surface emissivity ranges from 0.60 to 0.65. The power to each foil heater is controlled and regulated by a separate variac power supply. Energy balances, performed on each heated segment of the swirl chamber cylinder, then allow determination of local magnitudes of the convective heat flux.

As the facility is prepared for measurements, frost build-up is minimized by lowering the air temperature to just below the dew point to condense all water vapor from the air within the facility. This liquid water is then drained from the facility. Air temperatures as low as −120°C are then obtained with additional cooling as the air continues to re-circulate through the closed-loop facility. The mixed-mean temperature of the air entering the swirl chamber is measured using five calibrated copper–constantan thermocouples spread across the cross-section of each inlet duct, just downstream of each nozzle. These locations are chosen for these measurements because temperature and velocity profiles are uniform across the duct, allowing simple determination of local mixed-mean temperatures. Mixed-mean temperature at each entrance to the cylinder is then determined after accounting for conduction losses through each inlet duct. With this approach, the ratio of cylinder inlet mixed-mean temperature to local wall temperature is as low as 0.60. The temperature ratio is changed by adjusting the inlet air temperature and the swirl chamber heat flux level prior to reaching steady-state conditions. All measurements are obtained when the swirl chamber is at steady-state, achieved when each of the temperatures from the 30 thermocouples (on the swirl chamber surface) vary by less than 0.1°C over a 10 min period.

2.2. Local Nusselt number measurement

Spatially-resolved temperature distributions along the swirl chamber concave surface are determined using infrared imaging in conjunction with thermocouples, energy balances, digital image processing, and in situ calibration procedures. To accomplish this, the infrared radiation emitted by the heated interior surface of the swirl chamber is captured using a VideoTherm 340 Infrared Imaging Camera, which operates at infrared wave lengths from 8 to 14 μm. Temperatures, measured using the 30 calibrated, copper–constantan thermocouples distributed along the swirl chamber surface adjacent to the flow, are used to perform the in situ calibrations simultaneously as the radiation contours from surface temperature variations are recorded.

This is accomplished as the camera views the test surface through a custom-made, cylindrical zinc-selenide window (which transmits infrared wave lengths between 6 and 17 μm). Reflection and radiation from surrounding laboratory sources are minimized using an opaque shield which covers the camera lens and the zinc selenide window. Frost build-up on the outside of the window is eliminated using a small

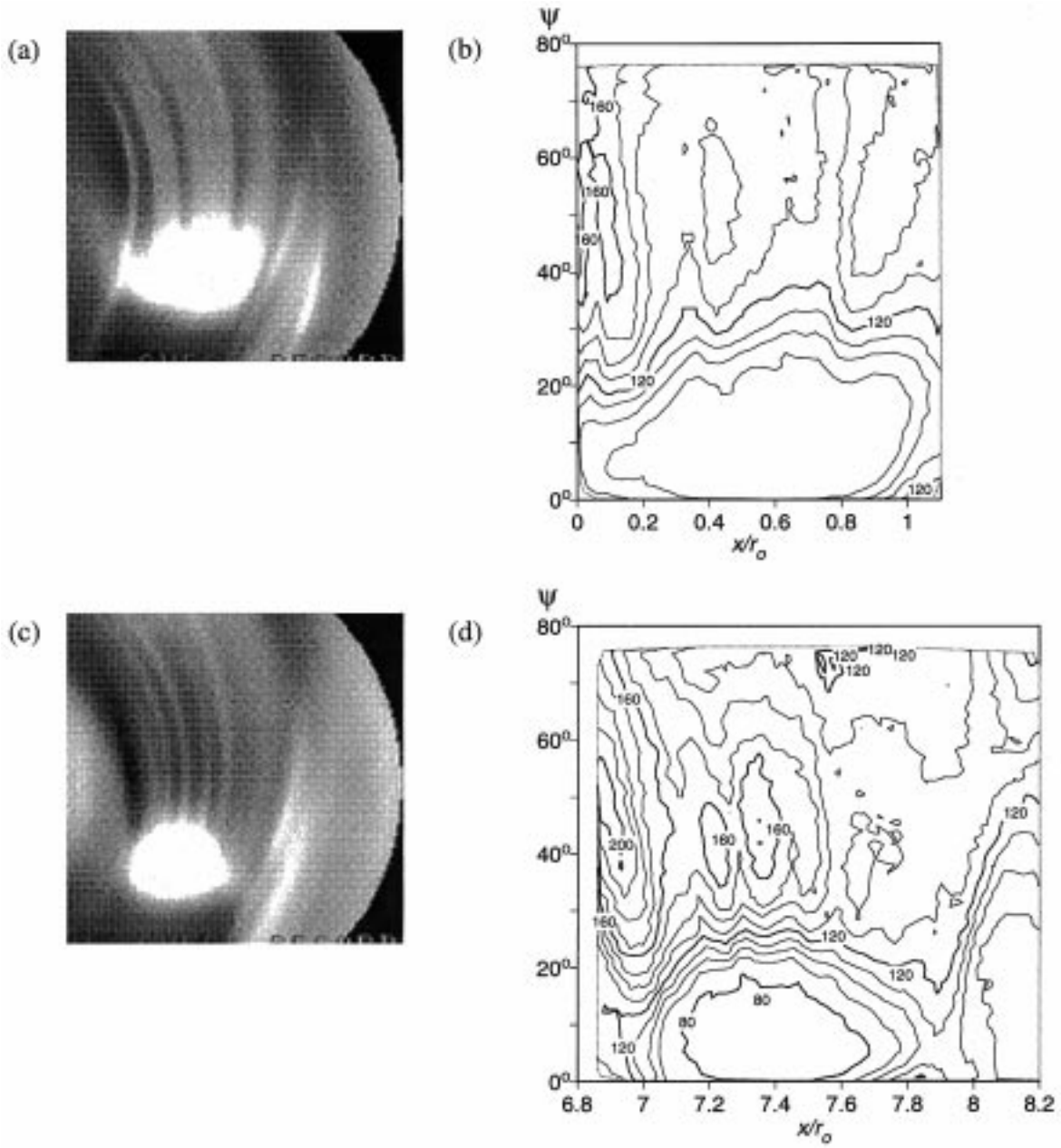

Fig. 2. Nusselt number distribution from infrared thermography measurements near inlet 1 (a) and (b), and near inlet 2 (c) and (d), for $Re = 12{,}150$, $T_i/T_w = 0.86$.

heated air stream from a hair dryer. The window is located on a segment of the swirl chamber which is either rotated or relocated axially so that the camera can view different portions of the interior surface of the swirl chamber. The exact spatial locations and pixel locations of these thermocouple junctions and the coordinates of a 12.7 by 12.7 cm field of view are known from calibration maps obtained prior to measurements. During this procedure, the camera is focused, and rigidly mounted and oriented relative to the test surface in the same way as when radiation contours are recorded.

With these data, gray scale values at pixel locations within video taped images from the infrared imaging camera are readily converted to temperatures. Because such calibration data depend strongly on camera

adjustment, the same brightness, contrast, and aperture camera settings are used to obtain the experimental data. The in situ calibration approach is advantageous because it rigorously and accurately accounts for these variations.

Images from the infrared camera are recorded as 8-bit gray scale images on commercial videotape using a Panasonic AG-1960 video recorder. Images are then digitized using NIH Image v1.60 software, operated on a Power Macintosh 7500 computer. Subsequent software is used to perform coordinate transformations to correct for non-rectangular, 'stretched', or distorted recorded images because of camera perspective or because camera lens orientation is not normal to the curved target surface. This software also converts each of 256 possible gray scale values to temperature at each pixel location using calibration data, and then determines values of local Nusselt numbers. Thermal conductivity in the Nusselt number is based on the average of the local wall temperature and the temperature of the air at the nearest upstream inlet. Contour plots of local surface temperature and Nusselt number (in 'unrolled' planar, Cartesian coordinates) are prepared using DeltaGraph v4.0 software. Each individual image covers a 300 by 300 pixel area. Data from 42 of these images are combined to produce the contour plot presented in Fig. 3.

2.3. Uncertainty estimates

Uncertainty estimates are based on 95 percent confidence levels, and determined using procedures described by Moffat [22]. Reynolds number uncertainty is ± 20. Uncertainty of temperatures measured with thermocouples is $\pm 0.15^{\circ}$C. Spatial and temperature resolutions achieved with infrared imaging are 0.8 mm and 0.2°C, respectively. Nusselt number uncertainty is then about ± 3.5.

3. Experimental results

Nusselt numbers are presented which show effects of varying Reynolds number at constant temperature ratio, and which show the effects of varying temperature ratio at constant Reynolds number. Reynolds number Re, based on inlet duct hydraulic diameter D_H and the inlet duct average velocity $\bar{U}$, ranges from 6100 to 19,600. The Reynolds number, based on the mean axial velocity through the swirl chamber $\bar{V}$ and swirl chamber diameter D, ranges from 2400 to 7200. Temperature ratio T_i/T_w, ranges from 0.60 to 0.95, and is based on the inlet temperature T_i, and on the local wall temperature T_w measured at the section of the swirl chamber farthest downstream, at $x/r_o = 14.0$–15.0.

Surface temperatures, required to determine the Nusselt numbers, are measured two ways. First, temperatures of the swirl chamber surface adjacent to the flow are determined with 30 thermocouples located at discrete locations along the surface. Secondly, surface temperatures are measured using infrared (IR) imaging. The IR technique provides a *continuous* temperature distribution along the surface (within the spatial discrimination of the camera, about 0.8 mm), whereas the thermocouples provide wall temperatures at discrete, local locations. These thermocouple data are also used for in situ calibration of each of the IR images, as mentioned earlier.

3.1. Local Nusselt number behavior near the swirl chamber inlets

Prior to discussing the variations of Nusselt number throughout the entire swirl chamber, Nusselt numbers, measured just downstream of each of the two inlets, are presented. Fig. 2 provides images measured using infrared thermography (IR) and contour plots of Nusselt number distributions near both inlets of the swirl chamber at $Re = 12{,}150$ ($Re_D = 4510$) and $T_i/T_w = 0.86$.

Fig. 2a, c shows unprocessed IR images, whereas Fig. 2b, d shows Nu distributions for the same spatial regions. Fig. 2a, b shows results from the swirl chamber surface nearest to inlet 1, and Fig. 2c, d shows results from the surface nearest to inlet 2. Recall that inlet duct 1 is located $x/r_o = 0$ to $x/r_o = 1$, and inlet duct 2 is located at $7.0 < x/r_o < 8.0$. The Nu contour plots contain data from the corresponding IR image, after spatial transformation to remove image distortions due to perspective and curvature are implemented. With these spatial transformations, each contour plot is viewed in a Cartesian plane. Each contour plot extends circumferentially from $\psi = 0^{\circ}$, the point at which each inlet duct is tangent to the swirl chamber, to $\psi = 80^{\circ}$, and axially over $0 < x/r_o < 1.1$ in Fig. 2b, and axially over $6.8 < x/r_o < 8.2$ in Fig. 2d.

Curved, lighter colored 'stripes' are evident in Fig. 2. Lighter-colored regions in each IR image correspond to higher surface temperatures and lower Nu, whereas darker regions indicate lower surface temperatures and higher Nu. Each Görtler vortex pair produces an upwash region and a downwash region. In the upwash region between the two vortices comprising each Görtler pair, higher temperature air from near the wall is moved away from the wall, producing a light stripe as the vortex pair advects in the positive ψ-direction. Each Görtler pair also has a downwash region on each side, in which lower temperature air is moved towards the wall, producing darker stripes as the vortices advect in the positive ψ-direction [23]. Both light and

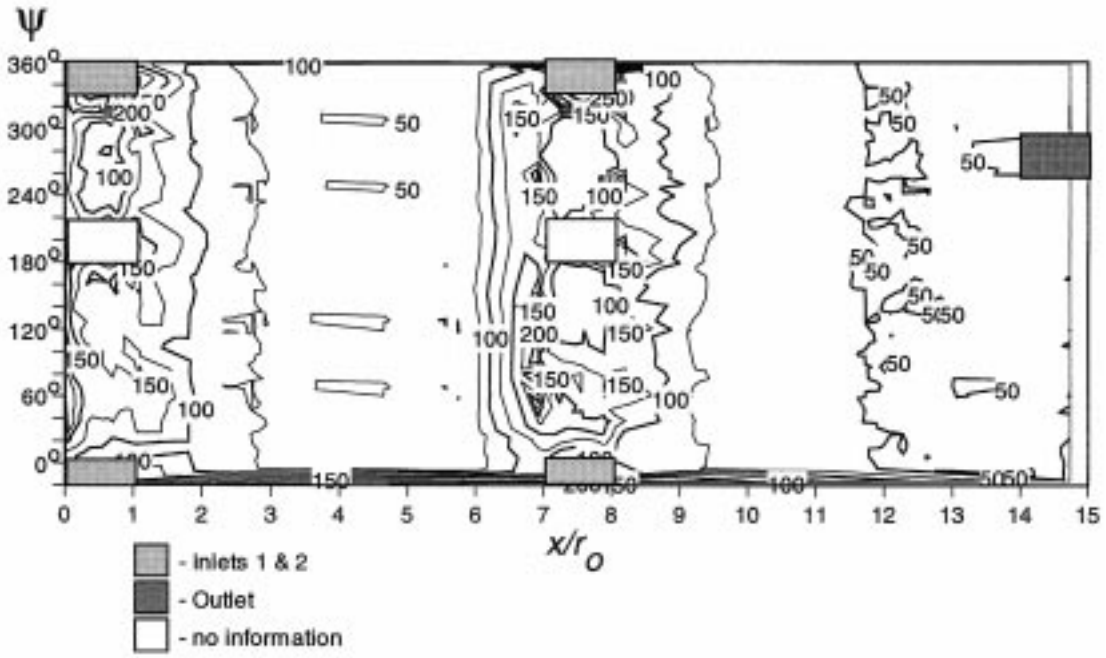

Fig. 3. Nusselt number distribution from infrared thermography measurements on interior surface of swirl chamber for Re = 12,150, $T_i/T_w = 0.86$.

dark curved stripes, due to Görtler vortex pairs, are seen near inlet 1 at $0.2 < x/r_o < 0.8$ and $30 < \psi < 60°$, and near inlet 2 at $7.3 < x/r_o < 7.8$ and $30 < \psi < 60°$. Fig. 2 thus also illustrates the excellent spatial resolution capabilities of the IR imaging and measurement system.

A common feature for each Re studied at $T_i/T_w = 0.86$ is the presence of a region of lower Nu (which corresponds to a lighter patch in each IR image), immediately downstream of each inlet. This is apparent in Fig. 2a, c as lighter regions near the bottom of the image. Fig. 2b indicates a corresponding oval contour level of Nu = 90, which covers the region $0.3 < x/r_o < 1.0$ and $0 < \psi < 22°$. A similar contour is evident in Fig. 2d at $7.15 < x/r_o < 8.15$ and $0 < \psi < 25°$. These regions are generally located at $\psi < 40°$, and correspond to locations upstream of initial Görtler vortex pair development. Structural connections between individual inlet ducts and the swirl chamber main cylinder may also share a small portion of the responsibility for the existence of these low Nu regions.

Regions of increased Nu appear in Fig. 2, near $x/r_o = 0.0$–0.1, $x/r_o = 0.9$–1.1, $x/r_o = 6.8$–7.1 and $x/r_o = 7.8$–8.2, for $25 < \psi < 70°$. Responsible are shear layer vortices, which develop within the shear layer on the upstream and downstream edges of the jet emanating from each inlet duct [23]. Near the upstream edge of inlet duct 2, at $x/r_o = 7$, this region extends from $x/r_o = 7.1$ and $\psi = 25°$, to $x/r_o = 6.8$ and $\psi = 60$–$70°$ because of the axial spreading of the flow from this duct. Similar spreading is not evident near inlet duct 1 because of the presence of the chamber end wall at $x/r_o = 0$.

3.2. Nusselt number behavior throughout swirl chamber

Fig. 3 shows contour plots of the Nusselt number as it varies along the entire interior concave surface of the swirl chamber for Re = 12,150 and $T_i/T_w = 0.86$. This is a composite of 42 separate IR camera views of the test surface, like the ones given in Fig. 2. In portions of the swirl chamber surface where axial gradients of Nu are small, Nu data are interpolated using DeltaGraph software. The data shown in Fig. 3 are presented in 'unrolled' in Cartesian coordinates, with horizontal axis x/r_o and vertical axis ψ. Several small regions are indicated on the plot where no data are provided. The light gray regions ($x/r_o = 0$–1 and $x/r_o = 7$–8) correspond to the locations of the inlet duct openings. The white regions ($x/r_o = 0$–1 and $x/r_o = 7$–8) indicate the locations of unused tangential ducts. Each of these is fitted with a contoured plug with a surface which matches the interior curvature of the swirl chamber. The dark gray region at $x/r_o = 14$–15 indicates the location of the radial exit duct of the swirl chamber. As mentioned, local Nusselt numbers are evaluated using thermal conductivities which are deter-

mined for each swirl chamber location using the average of inlet temperature T_i and local wall temperature T_w.

The largest variations of Nu in Fig. 3, as well as the largest magnitudes of Nu, are observed across the entire circumference $\psi = 0$–360°, near tangential inlets 1 and 2, between $x/r_o = 0$ and $x/r_o = 1$, and between $x/r_o = 7$ and $x/r_o = 8$, respectively. As axial position increases from $1.5 < x/r_o < 2.8$, Nu initially decreases and they become more uniform in the circumferential direction. Nusselt numbers are then nearly constant in both circumferential and axial directions for $2.8 < x/r_o < 6.0$ and $0 < \psi < 360^\circ$. At $x/r_o = 6.0$, influences of inlet 2 begin to affect the flow, and Nu increases as x/r_o increases from 6.0 to 7.0. At larger x/r_o, near inlet 2, surface Nu begin to vary in both axial and circumferential directions. As x/r_o becomes greater than 8.4–9.0 and the flow leaves the region of inlet 2, Nusselt numbers become more axially and circumferentially uniform until the end of the swirl chamber is reached at $x/r_o = 14.0$–15.0.

3.3. Axial development of circumferentially-averaged Nusselt numbers

Fig. 4 presents circumferentially-averaged Nu as they vary with x/r_o, determined both from thermocouples and from IR thermography, for Re = 12,150 and $T_i/T_w = 0.86$. Thermocouple data in Fig. 4 provide information at seven discrete axial locations. Each of these thermocouple Nusselt number data points is determined from an average of measurements made at three or four points around the circumference of the facility. Fig. 5 provides Nu data for a single temperature ratio $T_i/T_w = 0.86$ for Re = 6100, 12,150 and 19,200, while Fig. 6 provides Nu data taken at four different temperature ratios of $T_i/T_w = 0.86$, 0.60, 0.74 and 0.95, at Reynolds numbers from Re = 18,000 to 19,600. The IR data presented in Figs. 4–6 are determined from the results in Fig. 3 and similar results at the other T_i/T_w and Re, and thus provide a continuous measurement of surface Nu variation around the circumference of the swirl chamber. Up to 1300 IR measured data points are used for determination of the circumferentially-averaged Nu at each axial location.

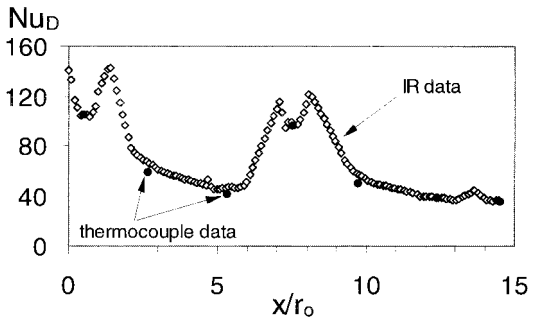

Fig. 4. Circumferentially-averaged Nusselt number distributions, Re = 12,150, $T_i/T_w = 0.86$.

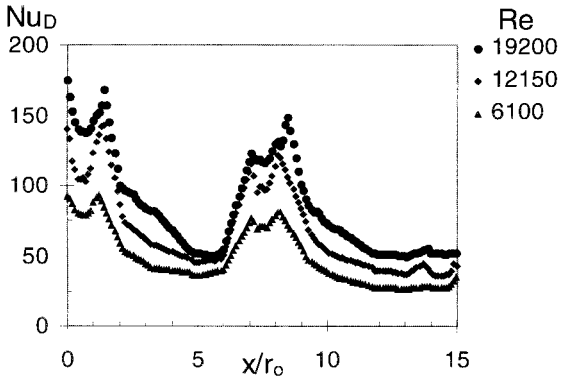

Fig. 5. Circumferentially-averaged Nusselt number distributions, Re = 6100–19,200, $T_i/T_w = 0.86$.

Local thermocouple and IR data are in excellent agreement when compared at the same x/r_o and ψ location. Small differences between *circumferentially-averaged* thermocouple and IR data are evident in Fig. 4 because thermocouple values are based on averages of only three or four discrete points, and thus provide an inaccurate Nusselt number circumferential average. In contrast, IR data provide a continuous distribution of the variation of Nu over the same surface, and thus, accurate circumferentially-averaged Nu at each ψ location.

In Fig. 4, Nusselt numbers are highest near the inlets at $x/r_o = 0$–1 and $x/r_o = 7$–8, then gradually decrease as flow advects away from the inlets. The higher Nu near the inlets are due to the presence of Görtler vortex pairs and shear layer vortices, as well as the interactions between these secondary flow structures.

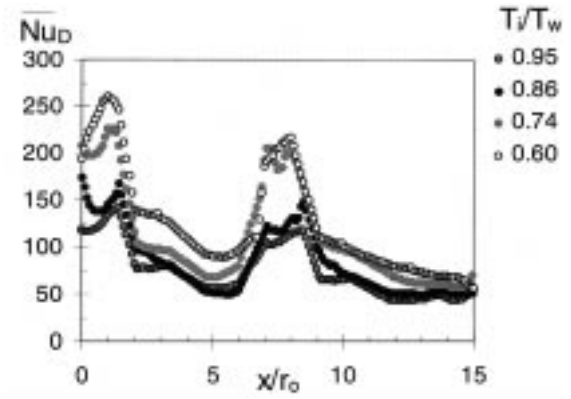

Fig. 6. Circumferentially-averaged Nusselt number distributions, Re = 18,000–19,600, $T_i/T_w = 0.60$–0.95.

In Figs. 5 and 6, *Nu* values are again highest near each inlet, at $x/r_o = 0$–1 and 7–8. Within each of these regions, for most experimental conditions, *Nu* values are especially high near $x/r_o = 0$ and $x/r_o = 7$. Values then decrease slightly near the centers of each inlet at $x/r_o = 0.5$ and 7.5, and then reach another local peak near $x/r_o = 1$ and $x/r_o = 8$. Nusselt numbers near inlet 2 are slightly lower than *Nu* near inlet 1 at all experimental conditions. As x/r_o increases beyond $x/r_o = 1$ and $x/r_o = 8$, *Nu* values decrease before becoming nearly constant at axial locations away from the inlets, at $x/r_o = 4$–5 and $x/r_o = 12$–14. Slight variations in circumferentially-averaged *Nu* are then observed near the exit duct at $x/r_o = 14$–15.

The peaks in circumferentially-averaged *Nu* near the inlets are due to the development of and interactions between Görtler vortices, and between Görtler vortices and shear layer vortices [23,24]. Higher *Nu* near each inlet are additionally due to development of a new thermal boundary layer, just downstream of each inlet duct. The local peaks in *Nu* just downstream of each inlet are believed to be due to vortices present in the shear layers produced at the edges of each jet emanating from each inlet duct. These vortices increase mixing between warmer fluid near the wall, and cooler fluid in the inlet jet. Centrifugal forces from helical fluid motion also force cold, denser fluid towards the warmer swirl chamber surfaces. In between these local peaks, slightly-lower, but still relatively high *Nu* are due to Görtler vortex pairs. The relatively high Nusselt numbers in the inlet regions also occur as the vortices oscillate in radial and axial directions. As *Nu* decreases at axial locations away from each inlet, the Görtler vortices near the internal concave surface become larger and display less-frequent interactions [4].

Circumferentially-averaged *Nu* for $Re = 6100$, 12,150 and 19,200, and for $T_i/T_w = 0.86$ in Fig. 5, increase with increasing *Re* at most axial locations. This is due primarily to increases in advection produced by increasing *Re*. For nearly all x/r_o, the increase in *Nu* is approximately the same between $Re = 6100$ and $Re = 12{,}150$ as it is between $Re = 12{,}150$ and $Re = 19{,}200$. At $x/r_o = 6$ between $Re = 19{,}200$ and $Re = 12{,}150$, the increase in *Nu* with increasing *Re* is less than for the same axial location comparing $Re = 6100$ and $Re = 12{,}150$.

Circumferentially-averaged *Nu* at $T_i/T_w = 0.60$, 0.74, 0.86 and 0.95, presented in Fig. 6, increase with decreasing T_i/T_w for most x/r_o, when compared at the same x/r_o. This increase occurs as centrifugal forces move cooler, denser air towards the heated wall. As a result, downwash regions within vortex pairs are lower in temperature and upwash regions are higher in temperature (relative to the local overall mixed-mean temperature). The increase in *Nu* as T_i/T_w decreases from $T_i/T_w = 0.95$ to 0.86 is much smaller than the *Nu* difference between $T_i/T_w = 0.86$ and 0.74 probably because centrifical forces exerted on the inlet air are higher as the density of the inlet air increases. Some circumferentially-averaged *Nu* characteristics at $T_i/T_w = 0.6$ are different than for higher T_i/T_w. For $T_i/T_w = 0.60$, peaks in *Nu* near the upstream edge of inlets 1 and 2, observed at higher T_i/T_w and associated with shear layer vortices, are not apparent. The absence of these peaks may be the result of density effects which have a more pronounced effect on Nusselt numbers than the 'mixing' produced by shear layer vortices and Görtler vortices.

3.4. Circumferential development of axially-averaged Nusselt numbers

Figs. 7–9 show Nusselt numbers as they vary with circumferential position ψ. The thermocouple data in Fig. 7 represent discrete, local measurements, and are given for seven axial locations and four circumferential locations. The *Nu* data, denoted '$0 < x/r_o < 1$' in Figs. 7–9, are determined from averages of IR data over $0.0 \le x/r_o \le 1.0$. Nusselt number data from axial averages of IR data across the entire swirl chamber are denoted '$0 < x/r_o < 15$' in Fig. 7.

As mentioned earlier, infrared data and thermocouple data agree well when compared at the same x/r_o and ψ location (as they must for the in situ calibrations). This is illustrated by the agreement between the '$0 < x/r_o < 1$' IR data and the $x/r_o = 0.5$ thermocouple data in Fig. 7 (when compared at the same ψ). Occasional small differences between these data sets are sometimes observed in Fig. 7 for the same reasons that differences between IR and thermocouple data exist in Fig. 4.

Fig. 7 additionally illustrates that Nusselt number data for $x/r_o = 0.5$ and $x/r_o = 7.5$ (obtained from thermocouple measurements) and IR data averaged over $0 < x/r_o < 1$ show important variations with ψ for all *Re* and T_i/T_w examined. These are due to the develop-

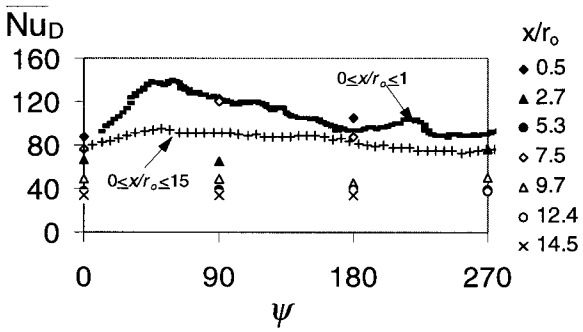

Fig. 7. Axially-averaged Nusselt number distributions, $Re = 12{,}150$, $T_i/T_w = 0.86$.

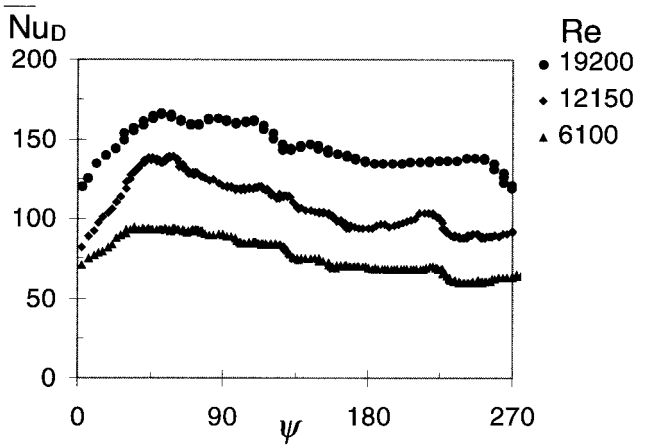

Fig. 8. Axially-averaged Nusselt number distributions, Re = 6100–19,200, $T_i/T_w = 0.86$.

ment of Görtler vortices on the interior concave surface of the swirl chamber. Circumferential variations of Nu are small, with only slight variations with ψ at $x/r_o = 2.7$, 5.3, 9.7, 12.4, and 14.5. Infrared Nu data obtained from averages over the entire axial length of the swirl chamber ($0 < x/r_o < 15$) also show only a small variation with circumferential position.

Axially-averaged IR Nu data, averaged over $0 < x/r_o < 1$, are plotted versus ψ in Fig. 8 for Re = 6100, 12,150 and 19,200 at $T_i/T_w = 0.86$. For each value of ψ, Nusselt numbers increase with increasing Re, because of larger advection with increasing Re. The differences in Nu at each ψ between Re = 6100 and 12,150 are approximately the same as the differences between data at Re = 12,150 and 19,200, when compared at the same ψ. At each Re presented, Nu values increase as ψ increases from $\psi = 0^\circ$ to $\psi = 45$–60°, then decrease slowly as ψ increases further to $\psi = 270^\circ$. The Nu change over $\psi = 0$–60° is due to the initial development of Görtler vortices and the development of a new thermal boundary layer just downstream of each inlet duct.

Fig. 9 presents IR Nu data, averaged over $0 < x/r_o < 1$ as they vary with ψ for $T_i/T_w = 0.60$, 0.74, 0.86 and 0.95 and Re ranging from 18,000 to 19,600. Nu increases with decreasing temperature ratio at each value of ψ. This increase is due to larger displacement and mixing of warmer air near the wall with larger amounts of cooler, denser air from the core region of the swirl chamber as T_i/T_w decreases. The increase in Nu at each ψ between $T_i/T_w = 0.95$ and $T_i/T_w = 0.86$ is somewhat smaller than the increase in Nu between temperature ratios 0.86 and 0.74, and between $T_i/T_w = 0.74$ and 0.60.

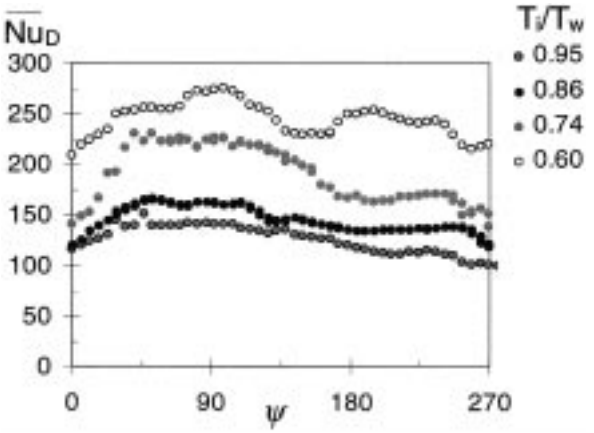

Fig. 9. Axially-averaged Nusselt number distributions, Re = 18,000–19,400, $T_i/T_w = 0.60$–0.95.

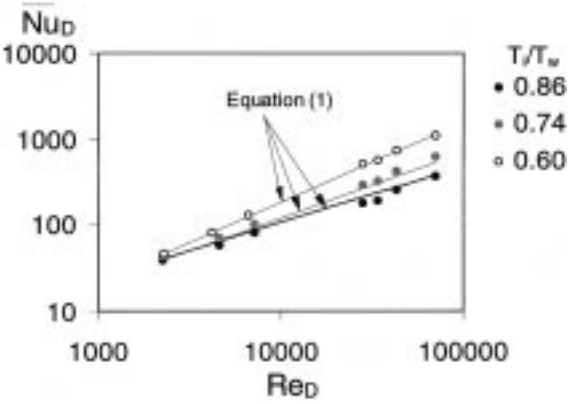

Fig. 10. Globally-averaged Nusselt numbers, from infrared thermography measurements, averaged over $0 < x/r_o < 15$ and $0 < \psi < 360^\circ$, and compared with Eq. (1).

3.5. Globally-averaged Nusselt numbers

Fig. 10 presents *Nu* data averaged over the entire swirl chamber interior surface, determined from results like the ones shown in Fig. 3, based on averages over $0 < x/r_o < 15$ and $0 < \psi < 360^\circ$. Here, globally-averaged *Nu* increase with increasing *Re*, and increase with decreasing T_i/T_w. Data for $T_i/T_w = 0.74$ and 0.60 and $Re > 20{,}000$ are determined by extrapolation based on differences between globally-averaged *Nu* data at other Re_D and at $T_i/T_w = 0.60$–0.95. For globally-averaged *Nu* over $0 < x/r_o < 15$ and $0 < \psi < 360^\circ$, the dependence of *Nu* on *Re* and T_i/T_w is given by an equation of the form

$$Nu_D = 0.63(T_i/T_w)^{5.7} Re_D^{0.56/(T_i/T_w)} \quad (1)$$

Eq. (1) shows a good match to experimental data in Fig. 10, for $2000 < Re_D < 80{,}000$ and $0.60 < T_i/T_w < 1.0$. Eq. (1) is used for $T_i/T_w > 0.86$ by setting $T_i/T_w = 0.86$.

4. Summary and conclusions

Nusselt number distributions are presented which show the effects of variations of temperature ratio and Reynolds number in a swirl chamber with two tangential inlets. Infrared imaging is used (in conjunction with thermocouples, energy balances and in situ calibrations) to obtain spatially-resolved distributions of local Nusselt numbers on the interior surface of the swirl chamber. Axially-averaged, circumferentially-averaged, and globally-averaged Nusselt numbers are determined from these local Nusselt number distributions.

Spatially-resolved Nusselt number distributions show complicated variations throughout the swirl chamber, especially near and just downstream of each swirl chamber inlet. The variations of *Nu* near the inlets are due to the presence of, and interactions between, Görtler vortex pairs and shear layer vortices. The Görtler vortex pairs and shear layer vortices produce characteristic light and dark parallel streaking in IR images. Such results illustrate the excellent accuracy and spatial resolution obtained with the infrared imaging techniques employed for the study. Because of the Görtler vortex pairs and shear layer vortices, Nusselt numbers are highest and show the largest axial and circumferential variations near the inlets. As the flows advect away from each inlet, Nusselt numbers decrease and become more spatially uniform along the interior surface of the chamber.

The spatially-averaged Nusselt numbers also show important variations with Reynolds number *Re*, temperature ratio T_i/T_w, non-dimensional axial location x/r_o, and circumferential location ψ. Local and spatially-averaged Nusselt numbers increase with decreasing temperature ratio when measured at the same spatial location and Reynolds number, at all experimental conditions studied ($T_i/T_w = 0.6$–0.95 and $Re = 6100$–19,200). Local and spatially-averaged Nusselt numbers also increase as *Re* increases, when measured at the same location and T_i/T_w temperature ratio. Circumferentially-averaged Nusselt numbers are highest and have the largest axial variation near the inlets, then decrease and become more uniform in the axial direction as flow moves away from the inlets. Axially-averaged Nusselt number distributions show the most important variations with ψ near and just downstream of each inlet. As flow moves away from these inlets, axially-averaged Nusselt numbers then become approximately circumferentially uniform and invariant with ψ.

Acknowledgements

The work presented in this paper was performed as a part of the Advanced Turbine System Technology Development Project, sponsored both by the US Department of Energy and Solar Turbines, Inc.

References

[1] F. Kreith, D. Margolis, Heat transfer and friction in turbulent vortex flow, Applied Science Research 8 (1959) 457–473.
[2] C.R. Hedlund, P.M. Ligrani, H.-K. Moon, B. Glezer, Heat transfer and flow phenomena in a swirl chamber simulating turbine blade internal cooling, ASME International Gas Turbine & Aeroengine Congress & Exhibition, Stockholm, Sweden, ASME Paper No. 98-GT-466, 1998.
[3] B. Glezer, T. Lin, H-K. Moon, An improved turbine cooling system, US Patent No. 5603606 ,1997.
[4] P.M. Ligrani, C.R. Hedlund, R. Thambu, B.T. Babinchak, H.-K. Moon, B. Glezer, Flow phenomena in swirl chambers, Experiments in Fluids 24 (3) (1998) 254–264.
[5] H-K. Moon, T. O'Connell, B. Glezer, Heat transfer enhancement in a circular channel using lengthwise continuous tangential injection, in: Proceedings of International Heat Transfer Congress, Seoul, South Korea, 1998.
[6] B. Glezer, H-K. Moon, J. Kerrebrock, J. Bons, G. Guenette, Heat transfer in a rotating radial channel with swirling internal flow, in: Proceedings of ASME 43rd International Gas Turbine and Aeroengine Congress and Exposition, Stockholm, Sweden, 1998.
[7] A.A. Khalatov, I.M. Zagumennov, Heat transfer and fluid dynamics near flat surfaces in confined swirling flows, in: Proceedings of the Ninth International Heat

Transfer Conference, Jerusalem, Israel, 1990, pp. 329–334.
[8] A.W. Date, Prediction of fully developed flow in a tube containing a twisted-tape, International Journal of Heat and Mass Transfer 17 (1974) 845–859.
[9] S.W. Hong, A.E. Bergles, Augmentation of laminar flow heat transfer in tubes by means of twisted-tape inserts, ASME Transactions—Journal of Heat Transfer 98 (1976) 251–256.
[10] W.F.J. Sampers, A.P.G.G. Lamers, A.A. Van Steenhoven, Experimental and numerical analysis of a turbulent swirling flow in a tube, ICHEME Symposium Series, 2(129), 765–771 (1992).
[11] H. Li, Y. Tomita, Characteristics of swirling flow in a circular pipe, ASME Transactions—Journal of Fluids Engineering 116 (1994) 370–373.
[12] J.B.W. Kok, F.J.J. Rosendal, J.J.H. Brouwers, LDA-measurements on swirling flows in tubes, SPIE Laser Anemometry Advances and Applications 2052 (1993) 721–728.
[13] R. Kumar, T. Conover, Flow visualization studies of a swirling flow in a cylinder, Experimental Thermal Fluid Science 7 (1993) 254–262.
[14] M. Dong, D.G. Lilley, Parameter effects on flow patterns in confined turbulent swirling flows, ASME FACT Computer Modeling, Cofiring and NOx Control 17 (1993) 17–21.
[15] H.H. Brunn, A. Fitouri, M.K. Khan, The use of a multiposition single yawed hot-wire probe for measurements in swirling flow, ASME FED Thermal Anemometry 16 (1993) 757–65.
[16] A. Fitouri, M.K. Khan, H.H. Bruun, A multiposition hot-wire technique for the study of swirling flows in vortex chambers, Experimental Thermal Fluid Science 10 (1995) 142–151.
[17] F. Chang, V.K. Dhir, Turbulent flow field in tangentially injected swirl flows in tubes, International Journal of Heat and Fluid Flow 15 (5) (1994) 346–356.
[18] W.R. Gambill, R.D. Bundy, An evaluation of the present status of swirl-flow heat transfer. ASME Paper No. 62-HT-42, 1–12 (1962).
[19] A.E. Bergles, Survey and evaluation of techniques to augment convective heat and mass transfer, International Journal of Heat and Mass Transfer 1 (1969) 331–413.
[20] R. Razgaitis, J.P. Holman, A survey of heat transfer in confined swirling flows, in: Future Energy Production Systems, Heat and Mass Transfer Processes, vol. 2, Academic Press, New York, 1976, pp. 831–866.
[21] P. Papadopoulos, D.M. France, W.J. Minkowycz, Heat transfer to dispersed swirl flow of high-pressure water with low wall super heat, Experimental Heat Transfer 4 (1991) 153–169.
[22] R.J. Moffat, Describing the uncertainties in experimental results, Thermal and Fluid Science 1 (1) (1988) 3–17.
[23] C.R. Hedlund, P.M. Ligrani, Local swirl chamber heat transfer and flow structure at different Reynolds numbers, ASME Transactions—Journal of Turbomachinery, to appear.
[24] R. Thambu, B.T. Babinchak, P.M. Ligrani, C.R. Hedlund, H.-K. Moon, B. Glezer, Flow in a simple swirl chamber with and without controlled inlet forcing, Experiments in Fluids 26 (3) (1999) 347–357.